Postprint of: Macek W, Branco R, de Jesus J, Costa J., Zhu S., Masoudi Nejad R., Gryguć A., Strain energy density and entire fracture surface parameters relationship for LCF life prediction of additively manufactured 18Ni300 steel, International Journal of Damage Mechanics (2024). © 2024 SAGE Publications. DOI: 10.1177/10567895241245879

Strain energy density and entire fracture surface parameters relationship for LCF life prediction of additively manufactured 18Ni300 steel

Journal:	*International Journal of Damage Mechanics*
Manuscript ID	IJDM-23-169.R1
Manuscript Type:	Original Research Paper
Date Submitted by the Author:	30-Nov-2023
Complete List of Authors:	Macek, Wojciech; Gdańsk University of Technology Branco, Ricardo; University of Coimbra, Department of Mechanical Engineering da Silva de Jesus, Joel Alexandre; University of Coimbra, DEM; IPL, DEM Costa, José; University of Coimbra, Department of Mechanical Engineering Zhu, Shun-Peng; University of Electronic Science and Technology of China, Department of Mechanical Engineering Masoudi Nejad, Reza; Xi'an Jiaotong University, Civil Engineering Gryguc, Andrew; University of Waterloo
Keywords:	18Ni300 steel, laser beam powder bed fusion, low-cycle fatigue, strain energy density, surface topography, entire fracture surface method
Abstract:	In this study, the connection between total strain energy density and fracture surface topography is investigated in additively manufactured maraging steel exposed to low-cycle fatigue loading. The specimens were fabricated using laser beam powder bed fusion (LB-PBF) and examined under fully-reversed strain-controlled setup at strain amplitudes scale from 0.3% to 1.0%. The post-mortem fracture surfaces were explored using a non-contact 3D surface topography measuring system and the entire fracture surface method. The focus is on the relationship between fatigue characteristics, expressed by the total strain energy density, and the fracture surface topography features, represented by areal, volume, and fractal dimension factors. A fatigue life prediction model based on total strain energy density and fracture surface topography parameters is proposed. The presented model shows good accordance with fatigue test results and outperforms other existing models based on the strain energy density. This model can be useful for post-failure analysis of engineering elements under low-cycle fatigue, especially for materials produced by additive manufacturing (AM).

SCHOLARONE™
Manuscripts

Strain energy density and entire fracture surface parameters relationship for LCF life prediction of additively manufactured 18Ni300 steel

Wojciech Macek [1] *, Ricardo Branco [2], Joel de Jesus [2], José Domingos Costa [2], Shun-Peng Zhu [3, 4], Reza Masoudi Nejad [5], Andrew Gryguć [6]

[1] Faculty of Mechanical Engineering and Ship Technology, Gdańsk University of Technology, Gabriela Narutowicza 11/12, 80-233 Gdańsk, Poland; wojciech.macek@pg.edu.pl

[2] CEMMPRE, ARISE, Department of Mechanical Engineering, University of Coimbra, 3030-788 Coimbra, Portugal; ricardo.branco@dem.uc.pt; joel.jesus@uc.pt; jose.domingos@dem.uc.pt

[3] School of Mechanical and Electrical Engineering, University of Electronic Science and Technology of China, Chengdu, P. R. China; zspeng2007@uestc.edu.cn

[4] Institute of Electronic and Information Engineering of UESTC in Guangdong, Dongguan 523808, China zspeng2007@uestc.edu.cn

[5] Faculty of Human Settlements and Civil Engineering, Xi'an Jiaotong University, China; masoudinejad@xjtu.edu.cn

[6] Department of Mechanical & Mechatronics Engineering, University of Waterloo, Waterloo, Canada; agryguc@uwaterloo.ca

* corresponding author: wojciech.macek@pg.edu.pl

For Peer Review

Abstract

In this study, the connection between total strain energy density and fracture surface topography is investigated in additively manufactured maraging steel exposed to low-cycle fatigue loading. The specimens were fabricated using laser beam powder bed fusion (LB-PBF) and examined under fully-reversed strain-controlled setup at strain amplitudes scale from 0.3% to 1.0%. The post-mortem fracture surfaces were explored using a non-contact 3D surface topography measuring system and the entire fracture surface method. The focus is on the relationship between fatigue characteristics, expressed by the total strain energy density, and the fracture surface topography features, represented by areal, volume, and fractal dimension factors. A fatigue life prediction model based on total strain energy density and fracture surface topography parameters is proposed. The presented model shows good accordance with fatigue test results and outperforms other existing models based on the strain energy density. This model can be useful for post-failure analysis of engineering elements under low-cycle fatigue, especially for materials produced by additive manufacturing (AM).

Keywords

18Ni300 steel; laser beam powder bed fusion; low-cycle fatigue; strain energy density; surface topography; entire fracture surface method.

Nomenclature and units

D_f	-	fractal dimension
N_f	cycles	number of cycles to failure
K'		cyclic hardening coefficient
n'		cyclic hardening exponent
R	-	strain ratio
R^2	-	coefficient of determination
Sq	mm	root mean square height
V	-	box volume
Vv	mm^3/mm^2	void volume
δ	-	box width
ΔW	MJ/m^3	strain energy density
ΔW^*	MJ/m^3	modified strain energy density
$\Delta\sigma/2$	MPa	nominal stress amplitude
$\Delta\varepsilon/2$	-	total strain amplitude
$\Delta\varepsilon_p/2$	-	plastic strain amplitude
$d\varepsilon/dt$	s^{-1}	strain rate

For Peer Review

1. Introduction

Metal-based additive manufacturing (AM) represents a group of processes that generally include powder bed fusion (PBF), directed energy deposition (DED), sheet lamination, and binder jetting. Within this group, laser beam powder bed fusion (LB-PBF) is currently one of the most versatile processes (J Li et al., 2019; Milewski, 2017; Newton et al., 2019) for production of complex 3D solid parts in a layer-by-layer fashion directly from CAD data (JN Li et al., 2019). So far, different materials have been successfully utilized. Among them, the 18Ni300 maraging steel, as a kind of low carbon iron-nickel alloy with high strength and toughness, has demonstrated to be appropriate for LB-PBF. Materials produced by this process have been often studied in order to evaluate not only the microstructure features but also the static mechanical response and the fatigue resistance (Avanzini, 2022; Garcias et al., 2021; Khosravani et al., 2020; Macoretta et al., 2022). In particular, fatigue durability is critical in most engineering applications subjected to cyclic loading. Thus, in order to develop reliable components, significant research has been conducted to establish a strong link between manufacturing parameters, population of defects, and fatigue performance. The response under low-cycle fatigue (LCF) loading is also a key issue because it provides fundamental information on the cyclic deformation maintenance of the materials which is pivotal when developing and implementing tuned fatigue life prediction models (Abdul-Latif, 2021; Cecchel et al., 2022; Romano et al., 2018; Zhu et al., 2012).

The fatigue damage is usually related with the load levels through stress-based (Liu and Pons, 2017; Macek and Mucha, 2017), strain-based (Chan et al., 2000; Skibicki and Pejkowski, 2017), or energy-based (stress-strain) models (Ahmadzadeh and Varvani-Farahani, 2019; Macek et al., 2017). Energy-based approaches, considering both stress and strain components, have a unifying character. In these approaches, fatigue life can be related with the dissipation energy, whose value can be determined from the field hysteresis loop in a strain-stress representation. Over the last decades, several interesting attempts have been made to evaluate the fatigue life of metallic materials under strain control mode using SED-based models (Branco, J.D. Costa, et al., 2021; Halford, 1966; Lachowicz, 2001; Li et al., 1998). Halford (Halford, 1966) investigated ferrous and non-ferrous metals and found that the strain energy density per cycle decreases as the strain amplitude increases, and that the relationship between the SED per cycle and the fatigue life can be established through a power function. Lachowicz (Lachowicz, 2001) present a method based on the integration of the history of the strain instantaneous power. Previous studies have investigated strain energy density models for evaluating fatigue life in metallic materials under strain-controlled conditions (Zhu et al., 2011). Several solutions were also used for the energy parameter calculated during a loading cycle and applied as the control signal for fatigue testing of the specimens (Macek and Macha, 2015; Mroziński and Boroński, 2007).

The experimental evaluation of surface topographies and fracture geometries is crucial for enhancing the comprehenasion of failure mechanisms and their relationship with the history of service loading. The development of surface metrology offers wide opportunities to investigate the failure mechanisms in many fields of engineering (Todhunter et al., 2017) as well as to better understand the topography characteristics (Podulka et al., 2023). The integrity valuation (Santus et al., 2022) ground on this particular analysis of fracture surfaces can provide valuable information about the damage background of the post-failure investigated component. Fracture surfaces caused by fatigue can be complex, requiring the analysis through the application of both standard surface topography parameters (International Organisation of Standardization, 2010; Podulka, 2021) and non-standard surface topography parameters, including fractal dimension (Bouchaud et al., 1990; Macek, 2019; Mandelbrot et al., 1984). Limited information exists regarding recommended parameters for characterizing fracture surfaces in additively manufactured metals, particularly LB-PBF maraging steel.

The motivation for this research is based on earlier studies that successfully connected different fatigue damage quantifiers with fracture surface topography parameters for various metallic materials and loading cases. Earlier studies by Macek et al. gave promising estimations of fatigue lifetime by correlating the stress amplitude (Macek, Robak, et al., 2022), strain amplitude (Macek et al., 2021; Macek, Pejkowski, et al., 2022) and strain energy density (Macek et al., 2023) with the 3D fractographic parameters. This paper explores the interdependency between total strain energy density (TSED) (Golos and Ellyin, 1988, 1989) and fracture surface topography features as an effective relationship to estimate the fatigue lifetime in LB-PBF 18Ni300 maraging steel under low-cycle fatigue (Branco et al., 2018). Fatigue life predictions are compared with results obtained from other strain energy density models, such as Lagoda-Macha (Łagoda, 2001), Neuber (Neuber, 1961), Molski-Glinka (Molski and Glinka, 1981), and Ye et al. (Ye et al., 2004).

2. Material and methods

The complete research program was organized into three main phases. Firstly, it was performed the LCF tests. Then, the SED calculations were performed. Finally, it was examined the fracture surfaces. The data gathered at each of these phases allows for a comprehensive investigation of fatigue life, considering both SED and fractographic considerations.

2.1. Low-cycle fatigue tests

The material employed in this research was 18Ni300 maraging steel manufactured by LB-PBF. Table 1 and Table 2 show, respectively, the elemental composition and the monotonic properties.

For Peer Review

Table 1. Elemental composition of LB-PBF 18Ni300 steel (Branco et al., 2018) (wt.%).

C	Ni	Mn	Co	Mo	Ti	Al	Cr	P	Si	Mn	Fe
0.01	18.2	0.65	9.0	5.0	0.6	0.05	0.3	0.01	0.1	0.04	balance

Table 2. Monotonic properties of LB-PBF 18Ni300 steel (Branco et al., 2018).

Porosity (%)	Density (g/m^3)	Hardness (HV1)	Young's Modulus (GPa)	Tensile Strength (MPa)	Yield Strength (MPa)	Strain at Failure (%)
0.74±0.09	7.42	354±5	168±29	1147±13	910±11	5.12±0.001

The specimen geometry, outlined in Figure 1, was printed through a Concept Laser M3 system. All specimens were printed in the same building batch considering a scanning scan speed of 200 mm/s, a hatch spacing of 100 μm, and a layer thickness of 40 μm. The deposition of the layers occurred vertically on the base plate, aligning with the direction of load application. After that, and prior to the fatigue tests, the gauge sections underwent mechanical polishing.

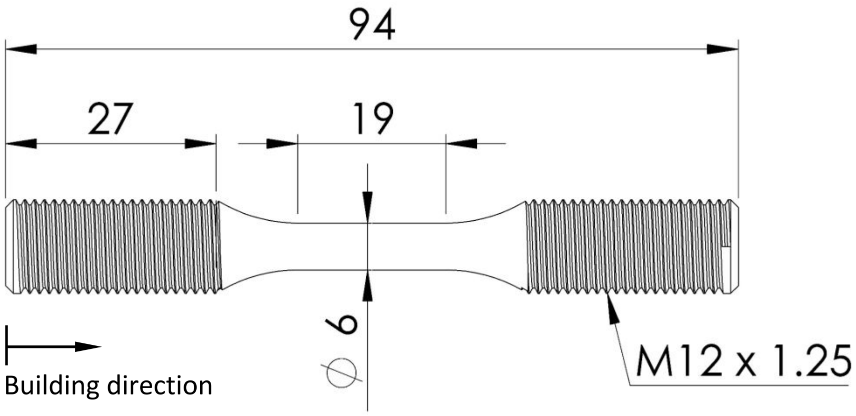

Fig. 1. Specimen geometry used in LCF tests (dimensions in mm) (Branco et al., 2018).

The LCF testing campaign was performed in a previous study designed by the research groups (Branco et al., 2018), in accordance with the ASTM E606 standard, on a conventional servo-hydraulic testing machine, 100 kN DARTEC model, under fully-reversed strain-controlled conditions with a strain ratio $R = -1$, sinusoidal waveforms, and a strain rate $d\varepsilon/dt = 8 \times 10^{-3}$ s^{-1}. The defined strain amplitudes were equal to 0.30%, 0.35%, 0.40%, 0.50%, 0.60%, 0.80%, 0.90%, and 1.0%.

The stress–strain data was collected using a mechanical extensometer, Instron 2620-601 model, with a gauge length of 12.5 mm, clamped to the gauge section of the specimen with two separated knife-edge attachements. This extensometer was linked to a digital data acquisition system and about 200 data points were recorded per cycle. Each specimen underwent a constant strain amplitude until reaching failure, and the fatigue tests finished when the specimens fractured into two separate pieces.

2.2. Energy-based approaches

Energy-based approaches represent the dissipated strain energy density per cycle which plays a central role in fatigue damage process. Regarding the strain energy density, if it is determined as the sum of the plastic SED and the elastic SED, it exhibits a unifying quality allowing the analysis of both the LCF and HCF regimes. Within the different approaches found in the literature, one of the most popular is the total strain energy density (TSED) concept proposed by Gołoś and Ellyin, see Figure 2 (Golos and Ellyin, 1988, 1989):

$$\Delta W_T = \Delta W_p + \Delta W_{e+} = \int_{cycle} \sigma_{ij} d\varepsilon_{ij}^{p} + \int_{cycle} \sigma_{ij} d\varepsilon_{ij}^{e} = \frac{1-n'}{1+n'}(\Delta\sigma - \delta\sigma_0)\Delta\varepsilon_p + \delta\sigma_0\Delta\varepsilon_p + \frac{1}{2E}\left(\frac{\Delta\sigma}{2} + \sigma_m\right)^2 \qquad (1)$$

where ΔW_{e+} is the elastic positive strain energy, ΔW_p is the plastic strain energy density, and *n'* is the cyclic hardening exponent.

The Ramberg-Osgood formula, which are the most common forms of describing the cyclic stress-strain response, is generally defined as follows (Ramberg and Osgood, 1943):

$$\Delta\varepsilon/2 = \frac{\Delta\sigma/2}{E} + \left(\frac{\Delta\sigma/2}{K'}\right)^{\frac{1}{n'}} \qquad (2)$$

where $\Delta\varepsilon/2$ is strain amplitude, and $\Delta\sigma/2$ is the stress amplitude, and *K'* is the cyclic hardening coefficient.

For Peer Review

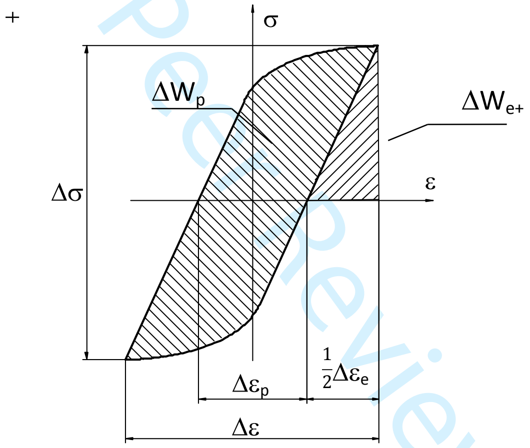

Fig. 2. Typical stress-strain hysteresis loop obtained under symmetrical loading conditions.

Other popular SED-based formulations are those introduced by Lagoda-Macha (W_{LM}) (Łagoda, 2001), Neuber (W_N) (Neuber, 1961), Molski and Glinka (W_{MG}) (Molski and Glinka, 1981), and Ye et al. (W_Y) (Ye et al., 2004). These formulations are briefly addressed below.

Lagoda-Macha's model accounts for the strain energy density applied in the component and is defined by Eq. (3).

$$W_{LM} = \frac{\left(\frac{\Delta\sigma}{2}\right)^2}{2E} + \frac{1-n'}{1+n'}\frac{\Delta\sigma}{2}\left[\frac{\frac{\Delta\sigma}{2}}{K'}\right]^{\frac{1}{n'}} \qquad (3)$$

Regarding the Neuber's model, it assumes that the energies generated in the material considering both an elastic and an elastic–plastic behaviour is the same and can be written by following equation.

$$W_N = \frac{\left(\frac{\Delta\sigma}{2}\right)^2}{2E} + \frac{\Delta\sigma}{4}\left[\frac{\frac{\Delta\sigma}{2}}{K'}\right]^{\frac{1}{n'}} \tag{4}$$

The equivalent strain energy density (ESED) according to Molski-Glinka (Molski and Glinka, 1981) can be determined using Eq. (5).

$$W_{MG} = \frac{\left(\frac{\Delta\sigma}{2}\right)^2}{2E} + \frac{\frac{\Delta\sigma}{2}}{1+n'}\left[\frac{\frac{\Delta\sigma}{2}}{K'}\right]^{\frac{1}{n'}} \tag{5}$$

Ye et al. (Ye et al., 2004) introduced a modified version of the ESED concept, which is defined through Eq. (6).

$$W_Y = \frac{\left(\frac{\Delta\sigma}{2}\right)^2}{2E} + \frac{2-n'}{2(1+n')}\,\frac{\Delta\sigma}{2}\left[\frac{\frac{\Delta\sigma}{2}}{K'}\right]^{\frac{1}{n'}} \tag{6}$$

For Peer Review

The strain energy density relationships used in this paper (see Eqs. 1, 3-6) are based on the cyclic hardening exponent (*n'*) and the cyclic hardening coefficient (*K'*) of the cyclic strain curve which is often generated under symmetrical tension-compression loading. These constants for the tested LB-PBF 18Ni300 maraging steel were determined in a previous study conducted by Branco et al. [33] and are equal to $n' = 0.1100$ and $K' = 1921.21$ MPa.

2.3. Fracture surface investigation

The fracture surfaces generated in the LCF tests were examined through a 3D non-contact measurement system, Mitutoyo Quick Vision Apex 302 model, using a 2× lens and a programmable light-emitting diode (LED) stage with coaxial lighting. The analysis was carried out considering a scale resolution of 0.1 µm, and it was used a linear encoder scale type. Fracture surface data were examined by means of MountainsMap software.

The entire fracture surface area was reduced to eliminate geometric discontinuities or missing points. In addition, this task was important to obtain similar dimensions for all specimens. The extracted areas are called here Region of Interest (ROI). Figure 3 shows a representative example of the original surface and the extracted surface for the fracture surface obtained at a total strain amplitude $\Delta\varepsilon/2 = 0.30\%$. The area considered in the analysis is marked with a circle over the entire surface shown on the left-hand side. On the right-hand side, it is shown the ROI, or in other words, the extracted area.

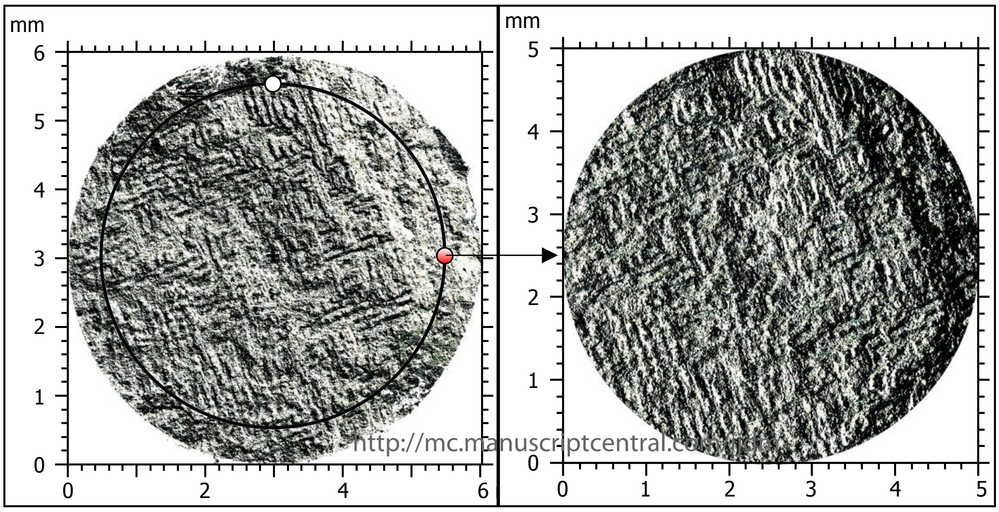

Fig. 3. Original and extracted fracture surface areas, fracture surface generated at $\Delta\varepsilon/2$ = 0.30%.

Fracture topography analysis was performed from fracture surface areas through either height parameters, *Sx*, or volume parameters, *Vx*. More specifically, in this study, the former was the root mean square height *Sq*, while the latter was the void volume *Vv*. These two parameters were calculated according to the ISO 25178-2 standard (ISO - ISO 25178-2:2012 - Geometrical product specifications (GPS) — Surface texture: Areal — Part 2: Terms, definitions and surface texture parameters, n.d.). The fracture surface features were also examined by applying the fractal dimension D_f.

In this study, the Enclosing Boxes Method (EBM) was applied. This method involves portioning the area into smaller segments, each with a width δ, and then determining the volume ($V\delta$) of all these segments covering the entire area. This is an iterative procedure which involves adjusting the width of the box, i.e. $\ln(V\delta)/\ln(\delta)$. In this analysis, an extra-fine resolution, with 96 points, was used.

For Pe

To estimate the fractal dimension D_f, a line is fitted using the least square method (LSM). The absolute value of the slope of this fitted line provides the value of the fractal dimension D_f. Fig. 4 shows a typical plot of the fractal dimension computed using the extra-fine resolution used in this analysis. This specific fracture surface corresponds to the specimen tested at $\Delta\varepsilon/2$ = 0.50%. D_f is determined based on the slope of one of the two regression lines that best fits the data. In this case, it can be seen that both regression lines have the same values (-2.220) with coefficients of determination R^2 = 1.000.

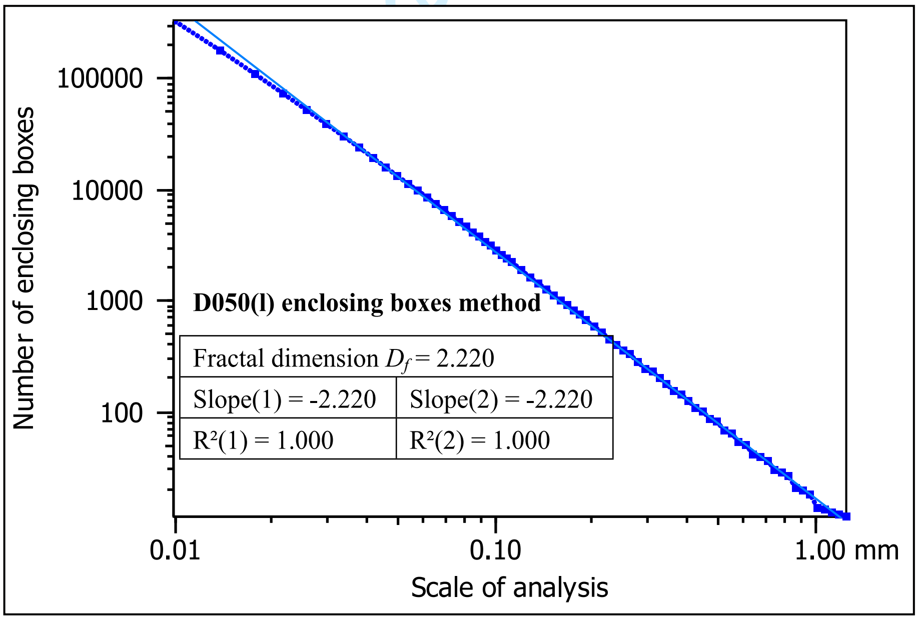

Fig. 4. Fractal analysis for the extracted area of the specimen tested at $\Delta\varepsilon/2$ = 0.50% performed using the EBM considering extra-fine resolution.

Another parameter utilized in the analysis fracture surface topography taken into account in this research is the texture isotropy. The directivity of the geometric surface texture depends on the fracture damage, and it is a consequence of the kinematics of the cracking process. On the other hand, isotropy in a material implies that it possesses the same physical or geometric properties in all directions. Similarly, isotropy in a surface indicates that the surface maintains the same structure properties in all directions. In essence, it exhibits a perfect symmetry in terms of material structure with respect to all axes of symmetry.

In the case under examination, as depicted in Fig. 5, the assessment of isotropy was carried out through an analysis of the autocorrelation function. Texture isotropy was used to gauge the directionality and periodicity of the topography, particularly its periodic patterns in two directions. Figure 5 shows the largest and the smallest values of the measured texture isotropy, obtained at a strain amplitude $\Delta\varepsilon/2$ = 1.00% (see Fig. 5(a)) and at a $\Delta\varepsilon/2$ = 0.50% (see Fig. 5(b)), respectively. For the former case, the circular and symmetrical function graph, typical of isotropic surfaces, resulted in an isotropy value exceeding 89%. On the other hand, in the latter case, the shape of texture isotropy function is asymmetric, slender, and elongated in one direction, which is associated with anisotropic surfaces. The isotropy in this case was approximately 44%. The results for all specimens are summarized in Table 3.

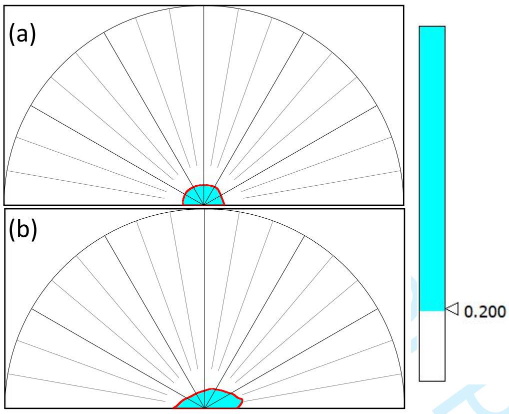

Fig. 5. Texture isotropy. Specimen subjected to (a) $\Delta\varepsilon/2$ = 1.00% (89.081%); and (b) $\Delta\varepsilon/2$ = 0.50% (43.960%).

Peer Review

3. Results and discussion

This section is divided into two subsections. The first subsection is focused on the topography characteristics of the fracture surface, considering both standard and fractal parameters. The second subsection provides a comprehensive overview of the LCF behaviour and introduces a novel fractography-TSED-based model for predicting the fatigue lifetime.

3.1. Fracture surface features after LCF

Figure 6 exhibits the fracture topographies obtained in the LCF tests for the different strain amplitudes listed in Table 3.

Table 3. Loading scenarios and results for LCF and fracture surface measurements of the tested specimens.

Specimen	**Total strain amplitude, $\Delta\varepsilon/2$ (%)**	**Elastic strain amplitude, $\Delta\varepsilon_e/2$ (%)**	**Plastic strain amplitude, $\Delta\varepsilon_p/2$ (%)**	**Stress amplitude, $\Delta\sigma/2$ (MPa)**	**Number of cycles to failure, N_f**	**Root mean square height, *Sq* (mm)**	**Void volume, *Vv* (mm³/mm²)**	**Fractal dimension, D_f**	**Texture isotropy (%)**
D100	1.005	0.5975	0.4077	1005	33	0.348	0.452	2.262	89.081
D090	0.905	0.5891	0.3163	990.8	64	0.456	0.494	2.234	73.121
D080	0.807	0.5984	0.2087	1006.5	40	0.217066	0.214	2.316	78.962
D060	0.609	0.5442	0.0644	915.3	129	0.378	0.483	2.262	79.78
D050	0.511	0.4764	0.0349	801.3	145	0.321	0.5	2.261	43.96
D040	0.411	0.4035	0.008	678.7	1087	0.162	0.237	2.294	87.375
D035	0.362	0.3584	0.0034	602.8	2399	0.139957	0.166	2.288	85.596
D030	0.304	0.305	0.0012	512.9	5441	0.176	0.173	2.256	86.032

An isotropic surface, as referred to above, is a surface that has a uniform topographic feature in all directions. It can be stated that isotropy, if expressed as a percentage, can vary from 0% (completely anisotropic surface) to 100% (fully isotropic surface). Here, for the sake of simplicity, the following conventional division of the isotropic degree is assumed: < 20% - anisotropic surface; 20% - 80% - mixed structure; and > 80% - isotropic surface. The results indicate isotropic surface for half of the investigated specimens. The other four fractures have a mixed surface structure but remain close to the conventional isotropic limit.

From Table 3 it is also possible to infer that the *Sq, Vv,* D_f and isotropy results do not correlate well with the strain or the fatigue life. A brief analysis relating the above-mentioned parameters with N_f will be carried out in Section 3.2 (see Fig. 9).

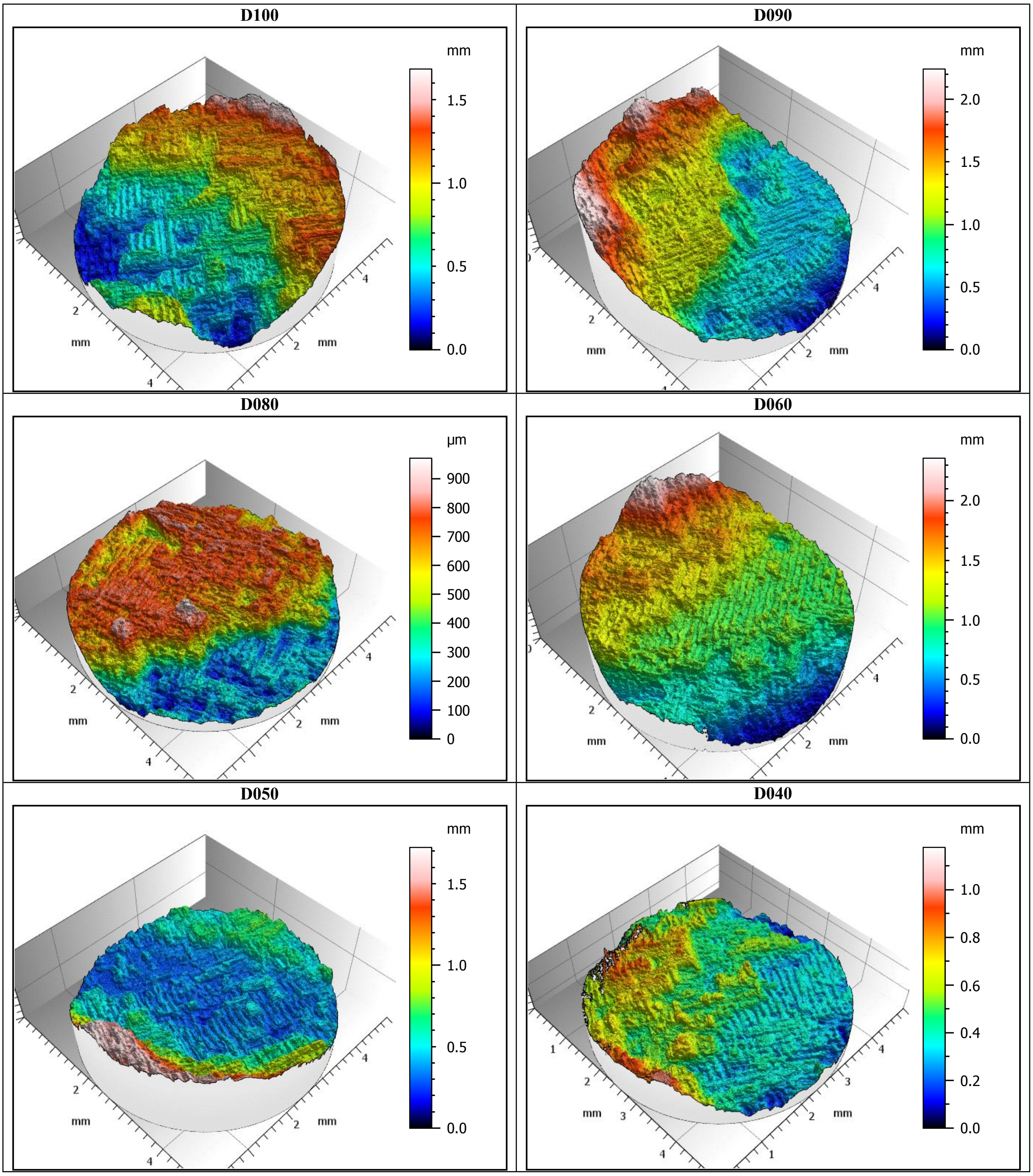

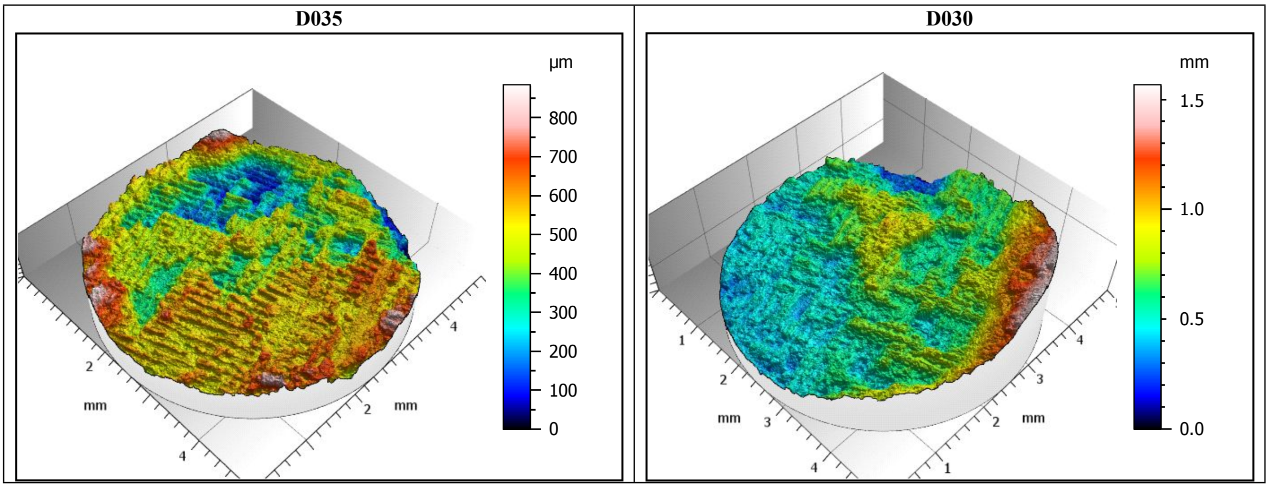

Fig. 6. Extracted fracture surfaces of different tested specimens (ROI).

For Peer

Both ductile and brittle fracture modes, with predominance of brittle fracture, can be noted in the material, as well as the existence of defects, which make it easier to develop microcracks. Figure 6 shows the texture of the fracture surface of the LB-PBF specimens. It is also possible to distinguish the shape and orientation of the particles deposited in each layer. This appearance is related to the microstructure and is an intrinsic feature of the manufacturing process. The optical micrograph (OM) in the longitudinal section of the tested material is exhibited in Figure 7. This figure reveals a coherent microstructure composed of elongated grains measuring approximately 150 µm in length and 30–35 µm in width.

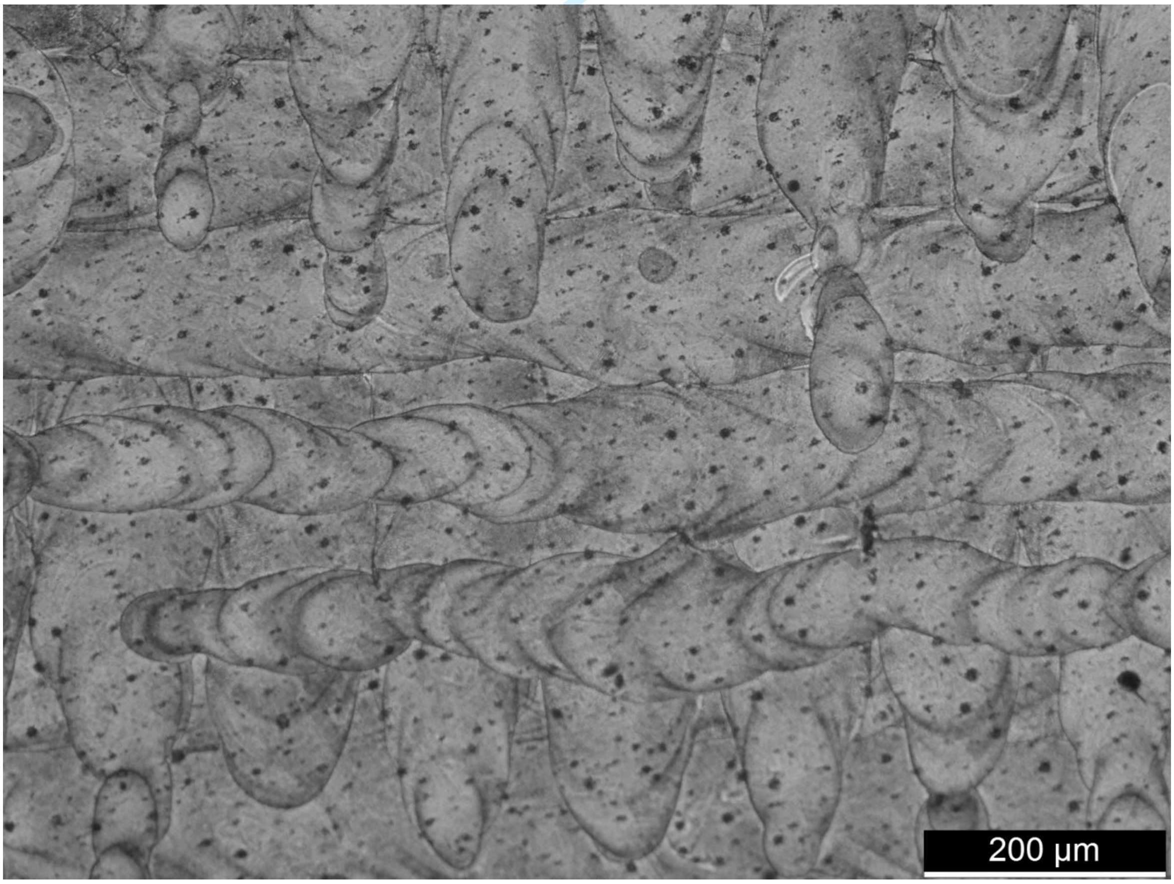

Fig. 7. OM of the LB-PBF 18Ni300 steel at magnifications of 100×.

Additionally, in order to verify the identity of the surface topography, the fractures of both sides of the broken specimens were juxtaposed. Fig. 8 exhibits the results of selected fracture surface topography parameters for the shorter portion of the broken specimens, which are marked as "S", and for the longer portions of the broken specimens, which are marked as "L". The presented data show that the measurements of both sides of the broken specimens can be used interchangeably. It is also visible that higher values of root mean square height *Sq* (Fig. 8(a)) and void volume *Vv* (Fig. 8(b)) are associated with lower values of $\Delta\varepsilon/2$. On the contrary, the values of fractal dimension D_f (Fig. 8(c)) and isotropy parameters (Fig. 8(e)) are lower at higher values of $\Delta\varepsilon/2$.

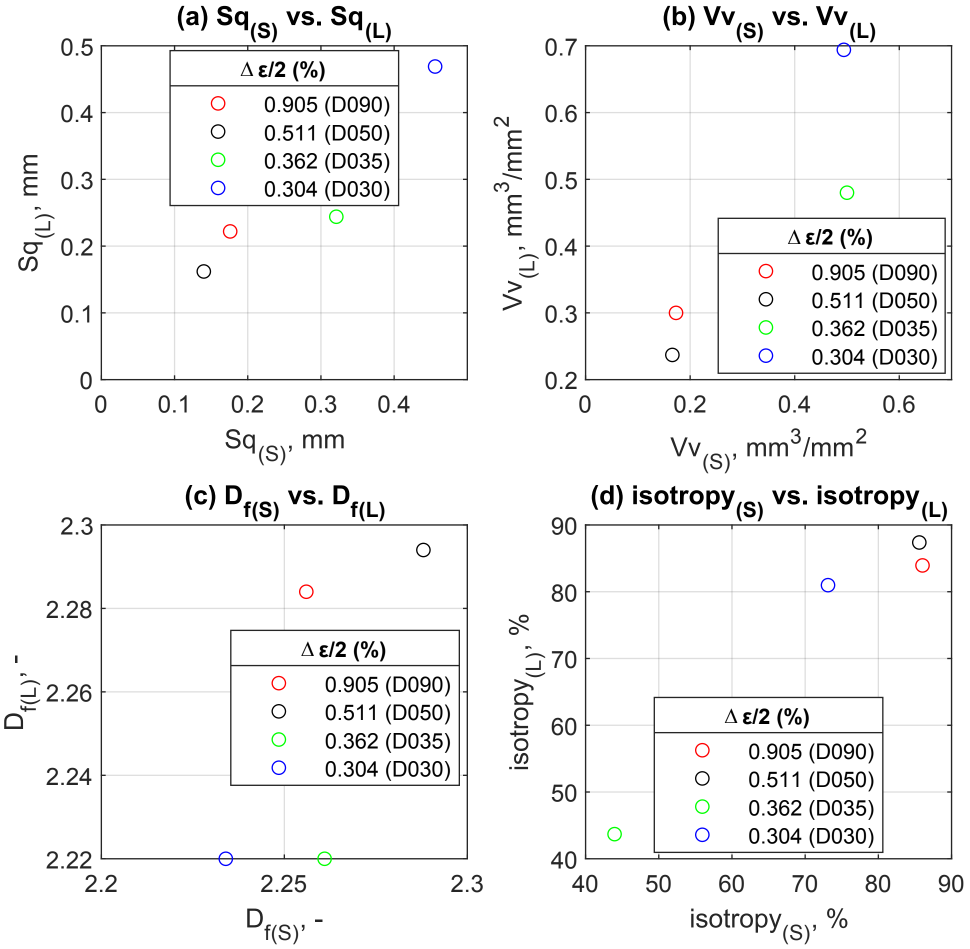

Fig. 8. Reciprocal relationship of the used surface topography parameters evaluated from the fracture surfaces of the shorter side and the longer sides of the broken specimens: (a) *Sq*; (b) *Vv*; (c) D_f; and (d) isotropy. S denotes the shorter part of broken specimen and L denotes the longer part.

3.2. Fatigue life prediction

Figure 9 presents the relationship between the total strain amplitude $\Delta\varepsilon/2$ and the fatigue life N_f (Figure 9(a)), as well the relationship between the stress amplitude $\Delta\sigma/2$ and the fatigue life N_f (Figure 9(b)). By examining the scatter bands (SB), we can draw the conclusion that the stress amplitude $\Delta\sigma/2$ fits more closely the data than the total strain amplitude $\Delta\varepsilon/2$. Nevertheless, this scatter is in line with the typical results found for additively manufactured metals under LCF loading.

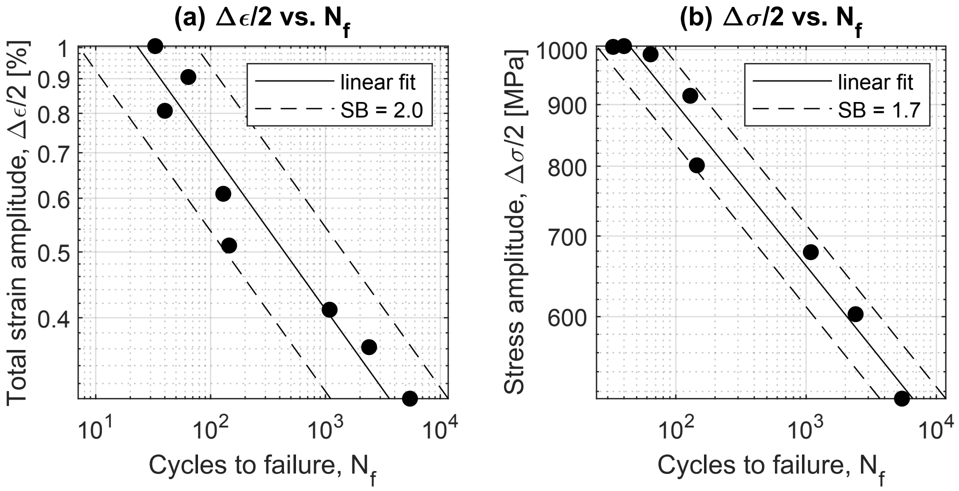

Fig. 9. Linear fit relationship between: (a) $\Delta\varepsilon/2$ and N_f; (b) $\Delta\sigma/2$ and N_f.

For Peer Review

Figure 10 shows the variation of the total strain energy density (TSED) per cycle, see Eq. (1), defined by the sum of the plastic and tensile elastic positive components (Branco et al., 2018). The TSED values are plotted on a base-10 logarithmic scale while the number of cycles N are presented in a dimensionless form, i.e. divided by the fatigue life N_f. Overall, it is clear from the figure that the total strain energy density is quite stable throughout the entire lifetime. Only for the specimen D035, for which the plastic strain amplitude is quite small, there was a slightly softening response during the first 10% of the test. Overall, irrespective of strain amplitude, the tested steel exhibited a saturated region up to 90% of the test. In the final stage, it was observed a decrease of total strain energy density energy before the final fracture, particularly at smaller strain amplitudes (specimens D030, D035 and D040). Considering this stable response, the mid-life cycle of each test was assumed to representative of the stable behaviour at this specific strain amplitude. Table 4 lists the TSED values (see Eq.(1)) obtained from the mid-life cycle as well as the values of strain energy density calculated using the other approaches (Eqs. 3-6).

Table 4. Strain energy density values calculated for the mid-life cycle

Specimen	ΔW_T (MJ/m³)	ΔW_{LM} (MJ/m³)	ΔW_N (MJ/m³)	ΔW_{MG} (MJ/m³)	ΔW_Y (MJ/m³)
D100	14.803	5.234	4.396	5.510	5.372
D090	11.743	4.852	4.125	5.090	4.971
D080	8.703	5.277	4.426	5.557	5.417
D060	3.988	3.360	3.034	3.468	3.414
D050	2.501	2.138	2.052	2.166	2.152
D040	1.561	1.413	1.397	1.419	1.416
D035	1.205	1.094	1.089	1.096	1.096
D030	0.863	0.785	0.785	0.786	0.786

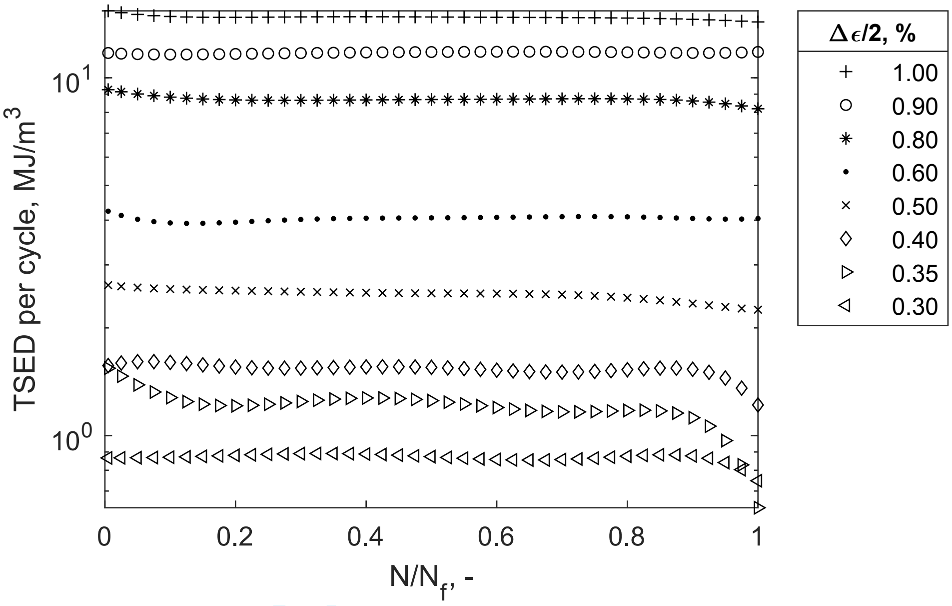

Fig. 10. TSED per cycle against the number of loading cycles at various strain amplitudes (Branco et al., 2018; Branco, J. D. Costa, et al., 2021).

Figure 11 plots fracture surface topography parameters against fatigue life. As can be seen, the values of *Sq* (Fig. 11(a), *Vv* (Fig. 11(b)), D_f (Fig. 11(c)), and isotropy (Fig. 11(d)) do not exhibit satisfactory correlation for all the tested specimens.

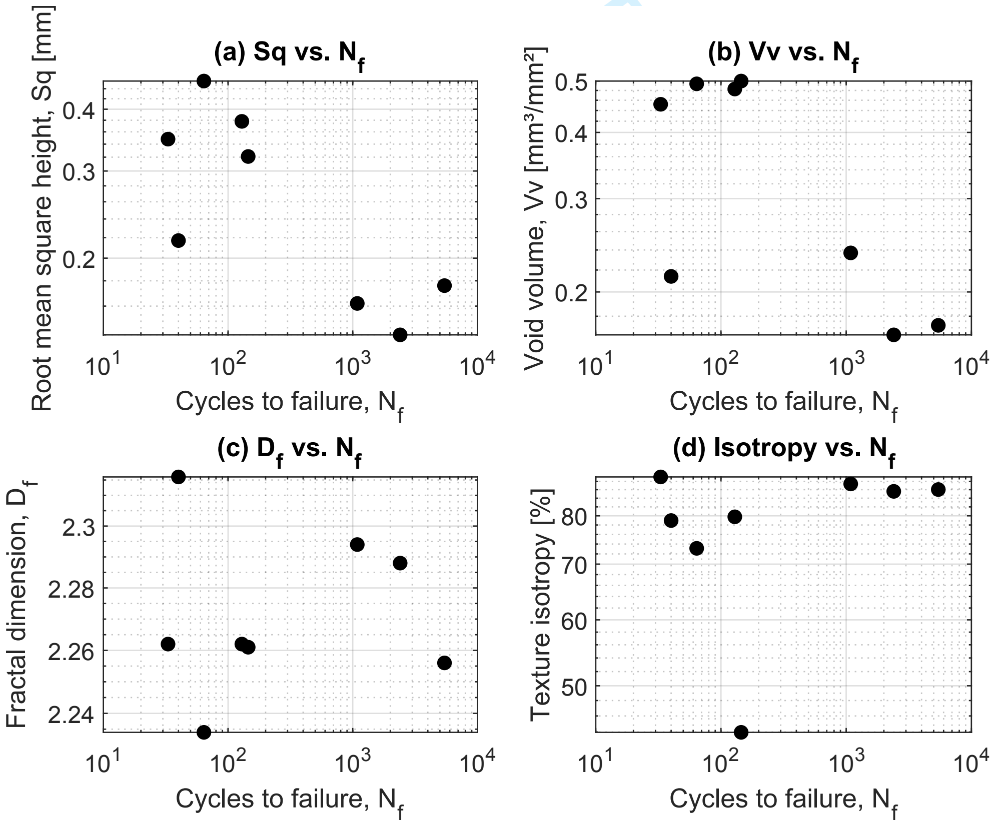

Fig. 11. (**a**) Root mean square height *Sq* versus fatigue life N_f; (**b**) Void volume *Vv* versus fatigue life N_f; (**c**) fractal dimension D_f versus fatigue life N_f; (**d**) isotropy versus fatigue life N_f.

To address this challenge, it is suggested to combine the most suitable surface topography parameters with other fatigue-related quantities, including energy-based parameters. In this manner, a more consistent method for estimating fatigue lifetime can be established. The proposed approach encompasses both the state of the fracture surface from a fractographic perspective and the stress-strain state. It can be expressed as follows:

$$W_T{}^* = W_T \times \frac{Vv \times Df}{Sq} \tag{7}$$

$$W_{LM}{}^* = W_{LM} \times \frac{Vv \times Df}{Sq} \tag{8}$$

$$W_N{}^* = W_N \times \frac{Vv \times Df}{Sq} \tag{9}$$

$$W_{MG}{}^* = W_{MG} \times \frac{Vv \times Df}{Sq} \tag{10}$$

$$W_Y{}^* = W_Y \times \frac{Vv \times Df}{Sq} \tag{11}$$

where *Vv* is the void volume, *Sq* is the root mean square height, and *Df* is the fractal dimension obtained for the entire fracture surface. The new post-failure equivalent topographic fracture factor seems to reflect the physical failure conditions of this material under fatigue. The modified strain energy density aims to identify the main governing quantities in order to reflect the physical meaning of the damaging process. The first quantity reflects the low-cycle fatigue loading history by accounting for the strain energy density. The second part represents the fracture surface energy through the combination of three fracture surface topography parameters ($\frac{Vv \times Df}{Sq}$). The unit is as follows: $\frac{[\frac{\mathrm{mm}^3}{\mathrm{mm}^2}] \times [-]}{[\mathrm{mm}]}$. Therefore, the modified strain energy density, ΔW^*, maintains the same unit, i.e. MJ/m^3.

A similar approach was successfully used by the authors (Macek et al., 2023) to assess the fatigue life in EN-AW 2024 aluminum alloys subjected to creep pre-strain and LCF loading. In this study, the fatigue life was predicted via the novel fracture surface state parameter, *P*, defined by the following expression:

$$P = \frac{VvD_f}{Sq}\varepsilon_a\sigma_a + \varepsilon_{creep}\sigma_{creep} \tag{12}$$

where ε_a is the strain amplitude, σ_a is the stress amplitude, ε_{creep} is creep strain, and σ_{creep} is creep pre-strain stress. The proposed novel fracture surface state parameter *P* is based on the strain energy (stress-strain relation). Regarding the physical significance of Eq. (12), it is divided into two main parts: the first accounts for the LCF history, including both the strain energy density and the fracture surface energy, represented by a combination of three fracture surface topography parameters ($\frac{VvD_f}{Sq}$); the second, related to the creep history, only considers the strain energy density component, because fracture does not occur.

For Peer Review

Table 5 presents the results of the modified TSED quantities and other energy parameters determined according to Eqs. 7-11.

Table 5. Modified values of SED calculated using fractographic quantities

Specimen	ΔW_T^* (MJ/m³)	ΔW_{LM}^* (MJ/m³)	ΔW_N^* (MJ/m³)	ΔW_{MG}^* (MJ/m³)	ΔW_Y^* (MJ/m³)
D100	43.491	15.378	12.914	16.188	15.783
D090	28.420	11.742	9.984	12.320	12.031
D080	19.871	12.049	10.105	12.687	12.368
D060	11.527	9.714	8.770	10.024	9.869
D050	8.808	7.528	7.228	7.627	7.577
D040	5.239	4.743	4.690	4.761	4.752
D035	3.270	2.970	2.956	2.974	2.972
D030	1.914	1.742	1.740	1.742	1.742

Fig. 12 plots both the SED values and the modified SED values against the fatigue life. The data were fitted through linear functions on log-log scales, i.e. through power functions. A statistical examination, utilizing the upper and the lower scatter bands, was also conducted. Overall, linear functions correlated well with the results of the modified strain energy density *W**. It is important to highlight that all tested cases led to values within 1.5 scatter bands. On the other hand, the analysis using the energy parameters yielded results within 2.1 and 1.7 (1.7 for W_T) scatter bands. Concerning the SED-based models, it is clear that their accuracy levels are rather similar.

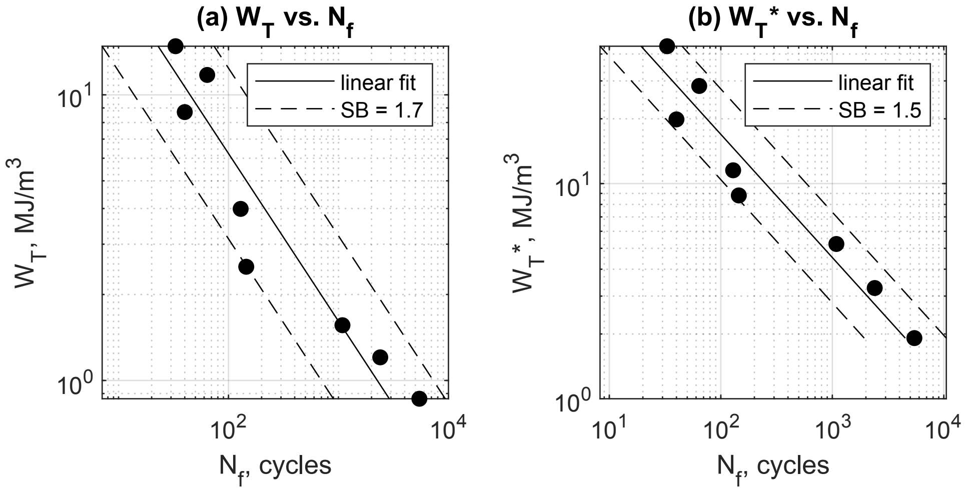

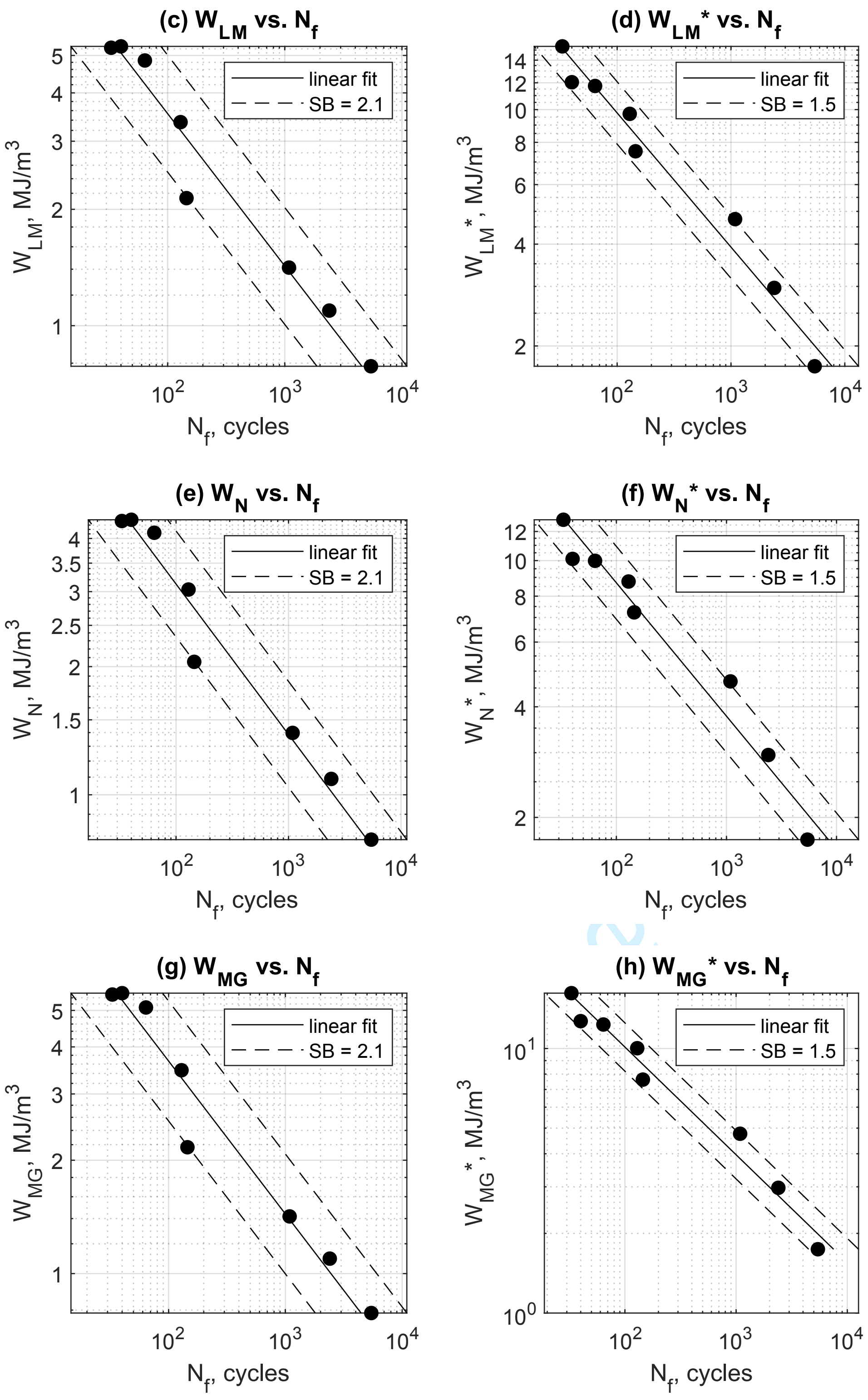
(c) W_{LM} vs. N_f
W_{LM}, MJ/m^3
N_f, cycles
linear fit
SB = 2.1
(d) W_{LM}^* vs. N_f
W_{LM}^*, MJ/m^3
N_f, cycles
linear fit
SB = 1.5
(e) W_N vs. N_f
W_N, MJ/m^3
N_f, cycles
linear fit
SB = 2.1
(f) W_N^* vs. N_f
W_N^*, MJ/m^3
N_f, cycles
linear fit
SB = 1.5
(g) W_{MG} vs. N_f
W_{MG}, MJ/m^3
N_f, cycles
linear fit
SB = 2.1
(h) W_{MG}^* vs. N_f
W_{MG}^*, MJ/m^3
N_f, cycles
linear fit
SB = 1.5
10^2
10^3
10^4
10^0
10^1

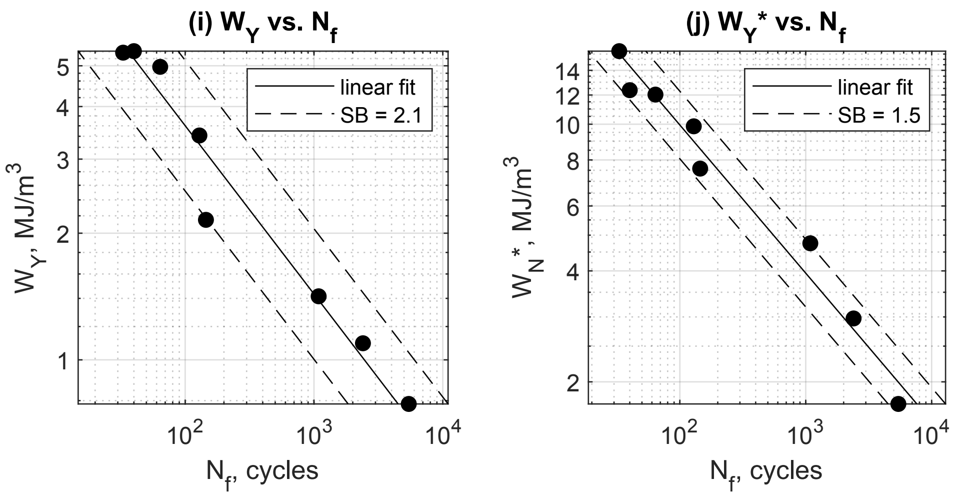

Fig. 12. Linear relationship between strain energy density and fatigue life: (a) W_T; (c) W_{LM}; (e) W_N; (g) W_{MG}; and (i) W_Y. Linear relationship between modified strain energy density and fatigue life: (b) W_T^*; (d) W_{LM}^*; (f) W_N^*; (h) W_{MG}^*; and (j) W_Y^*.

For Peer Review

Comparing the TSED values with other energy-based parameters (see Table 4), we notice that W_T reaches its peak at highest strain amplitude, i.e. $\Delta\varepsilon/2$ = 1.00% (D100), while the other parameters attain the maximum values at the highest stress amplitude, i.e. $\Delta\varepsilon/2$ = 0.80% (D080). However, the same analysis performed with the modified strain energy density parameters W^* shows that the highest values for all modified parameters occurred for the specimen with the largest strain amplitude, i.e. $\Delta\varepsilon/2$ = 1.00% (D100). Furthermore, it is also evident for all modified parameters, except for W_T^*, that the energy-based values for the specimen D090, i.e. $\Delta\varepsilon/2$ = 0.90%, are lower than those for the specimen D080, $\Delta\varepsilon/2$ = 0.80%.

Taking into account the characteristics discussed earlier regarding W_T (before and after the modification with surface topography parameters) and its consistency under constant strain levels over time (see Fig. 10), W_T^* was chosen for subsequent analysis in predicting the fatigue life. The relationship between the fatigue life N_{fcal} and the proposed modified parameter W_T^* can be defined through Eq. (13).

$$N_{fcal} = 16290 \times (W_T^*)^{-1.676} \tag{13}$$

Figure 13 compares the relationship between N_f and W_T as well as between the N_{fcal} and W_T^*. It can be seen that the values of total strain energy density show higher scatter than those obtained from the modified TSED. The fatigue life model N_{fcal} was validated from the measured data (red circles) and the main statistical parameters listed in Table 6.

Table 6. General power model (Eq. 13) goodness of fit.

SSE	137100
R^2	0.9947
RMSE	151.2

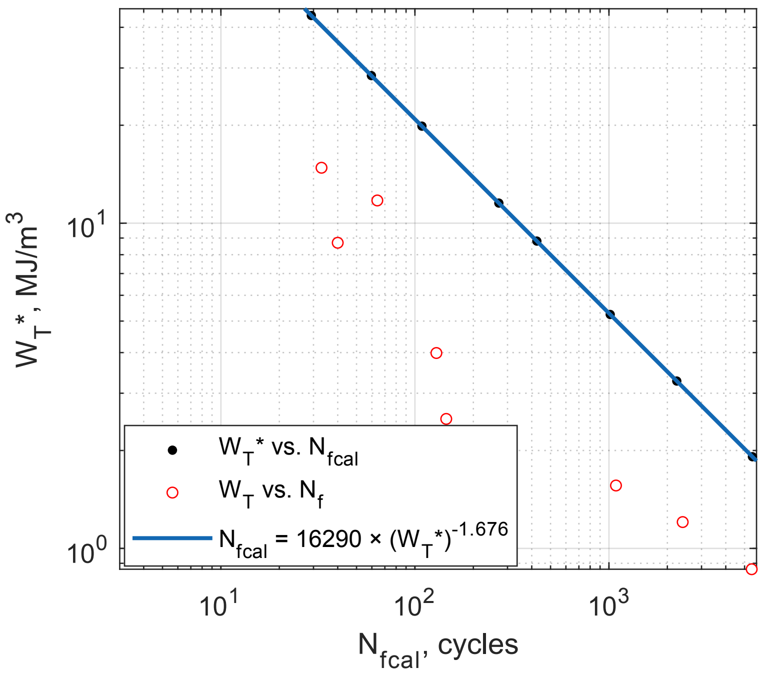

Fig. 13. Fit plot W_T^* and fatigue life N_{fcal} (black dots) validated by W_T and fatigue life N_f data (red circles).

Based on Fig. 14, it is evident that the calculations align closely with the experimental findings. This is illustrated by the fact that the values for all the tested cases are contained within a 1.5 scatter bands. The fitted data exhibit a variance of 0.0602 and a standard deviation of 0.2454.

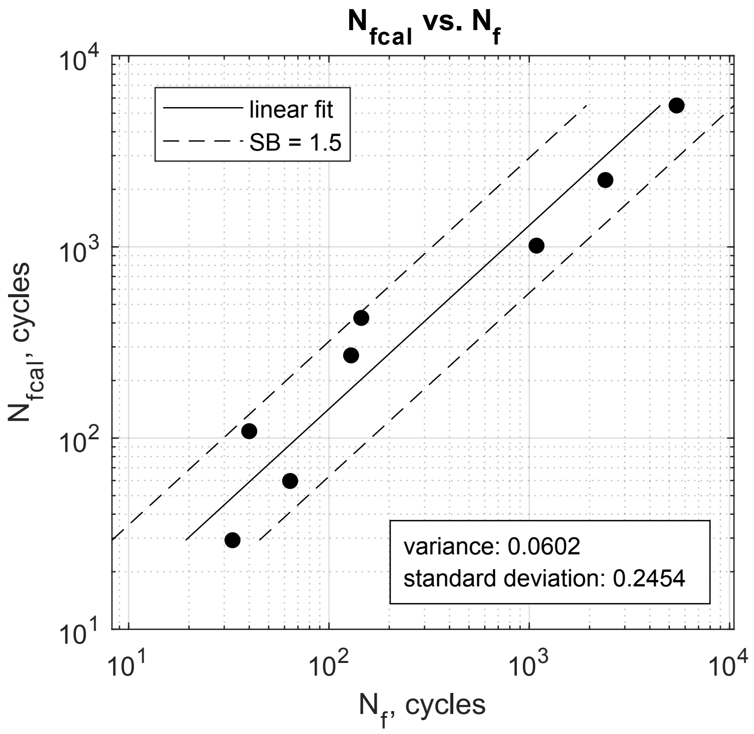

Fig. 14. Experimental fatigue life (N_f) versus calculated fatigue life (N_{fcal}).

3.3. Fractographic observations section

It is recommended to use various measurement methods and scales of analysis in the study of the shape of fracture surfaces. In this way, it is possible to obtain complete information on fracture formation and failure mechanisms. The fracture surfaces of the specimens were investigated by scanning electron microscope (SEM). In the observed areas, unmelted particles, cleavage facets and tear ridges were found (see Fig. 15). It can be noted, from previous observations, that the crack was initiated at the edge of the specimen. The propagation area was mainly dominated by a ductile mode of fracture characterized by ductile dimples, microvoids and secondary cracks that occurred due to the joining of the pores.

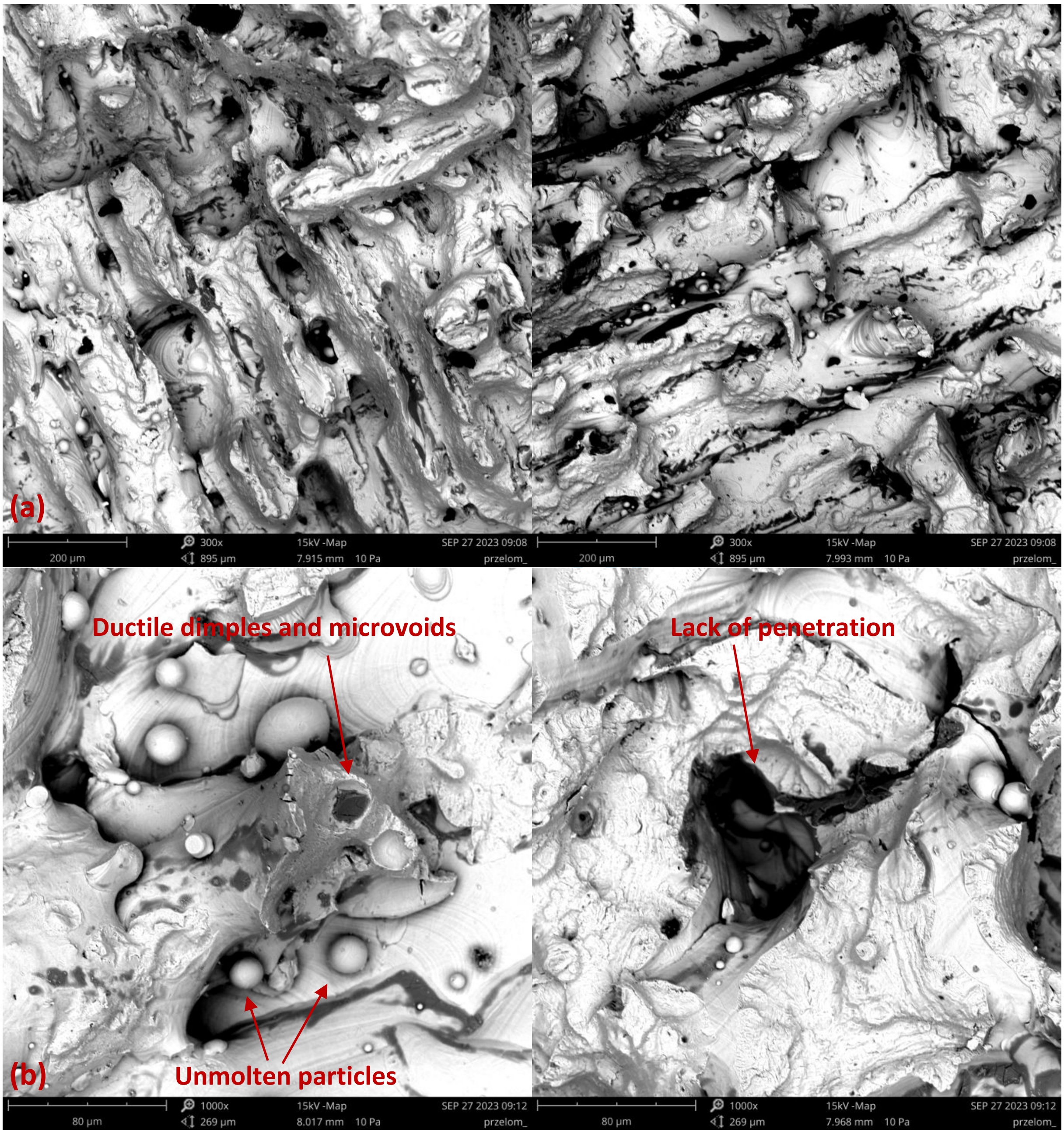

Fig. 15. Fractographs of the specimens tested under 1.00% strain amplitudes with (a) magnitude 300× and (b) 1000×.

4. Conclusions

In this paper, it is introduced a LCF life assessment model for LB-PBF 18Ni300 maraging steel combining both fracture surface topography parameters and total strain energy density. From the present study, the following conclusions can be drawn:

- The total strain energy density per cycle remained rather stable quantity throughout the entire life, regardless of the total strain amplitude;

- The total strain energy density at mid-life cycle combined with the entire fracture surface parameters showed a satisfactory relationship with the fatigue life, following a power-law;

- Predictions made using the TSED-based approaches fell within scatter bands of ±1.7, while those obtained from the modified TSED-based approach fell within narrower scatter bands of ±1.5;

- The orientation texture of fractures and the building direction resulted in isotropic fracture surface structures, with texture isotropy values ranging from 44% to 89%.

Entire fracture surface method has universal application, allowing the analysis of a wide range of engineering problems encompassing different materials, geometric configurations and loading histories. The same criterion is applied to all specimens. Due to the universality of surface metrological values, it is possible to adapt these methods to describe fatigue cracking processes in other material groups, such as non-metals. Especially this methodology holds promise for application in LCF life assessment for other additive manufactured metallic materials and can contribute to enhance the understanding of the fatigue failure kinetics.

For Peer Review

References

Abdul-Latif A (2021) Continuum damage model for low-cycle fatigue of metals: An overview. *https://doi.org/10.1177/1056789521991620* 30(7). SAGE PublicationsSage UK: London, England: 1036–1078.

Ahmadzadeh GR and Varvani-Farahani A (2019) Energy-based damage descriptions to assess fatigue life of steel samples undergoing various multiaxial loading spectra. *International Journal of Damage Mechanics* 28(1). SAGE Publications Ltd: 35–57.

Avanzini A (2022) Fatigue Behavior of Additively Manufactured Stainless Steel 316L. *Materials 2023, Vol. 16, Page 65* 16(1). Multidisciplinary Digital Publishing Institute: 65.

Bouchaud E, Lapasset G and Planès J (1990) Fractal Dimension of Fractured Surfaces: A Universal Value? *Europhysics Letters* 13(1). IOP Publishing: 73.

Branco R, Costa JDM, Berto F, et al. (2018) Low-cycle fatigue behaviour of AISI 18Ni300 maraging steel produced by selective laser melting. *Metals*. Epub ahead of print 2018. DOI: 10.3390/met8010032.

Branco R, Costa J.D., Borrego LP, et al. (2021) Comparison of different one-parameter damage laws and local stress-strain approaches in multiaxial fatigue life assessment of notched components. *International Journal of Fatigue* 151. Elsevier: 106405.

Branco R, Costa J. D., Martins Ferreira JA, et al. (2021) Multiaxial fatigue behaviour of maraging steel produced by selective laser melting. *Materials and Design* 201. Elsevier Ltd: 109469.

Cecchel S, Mohammad Javad Razavi S, Mega F, et al. (2022) Fatigue testing and end of life investigation of a topology optimized connecting rod fabricated via selective laser melting. *International Journal of Fatigue* 164. Elsevier: 107134.

Chan LC, Lee TC, Fan JP, et al. (2000) Formulation of a Strain Based Orthotropic Elasto-Plastic Damage Theory. *http://dx.doi.org/10.1177/105678950000900204* 9(2). Sage PublicationsSage CA: Thousand Oaks, CA: 174–191.

Garcias JF, Martins RF, Branco R, et al. (2021) Quasistatic and fatigue behavior of an AISI H13 steel obtained by additive manufacturing and conventional method. *Fatigue & Fracture of Engineering Materials & Structures* 44(12). John Wiley & Sons, Ltd: 3384–3398.

Golos K and Ellyin F (1988) A Total Strain Energy Density Theory for Cumulative Fatigue Damage. *Journal of Pressure Vessel Technology* 110(1). American Society of Mechanical Engineers Digital Collection: 36–41.

Golos K and Ellyin F (1989) Total Strain Energy Density as a Fatigue Damage Parameter. *Advances in Fatigue Science and Technology*. Springer, Dordrecht: 849–858.

Halford G (1966) The energy required for fatigue(Plastic strain hystersis energy required for fatigue in ferrous and nonferrous metals). *Journal of materials* 1: 3–18.

International Organisation of Standardization (2010) ISO 25178. *Geometric Product Specifications (GPS) – Surface texture: areal*.

ISO - ISO 25178-2:2012 - Geometrical product specifications (GPS) — Surface texture: Areal — Part 2: Terms, definitions and surface texture parameters (n.d.). Available at: https://www.iso.org/standard/42785.html (accessed 28 December 2020).

Khosravani MR, Berto F, Ayatollahi MR, et al. (2020) Fracture behavior of additively manufactured components: A review. *Theoretical and Applied Fracture Mechanics* 109. Elsevier B.V.: 102763.

Lachowicz CT (2001) Calculation of the elastic–plastic strain energy density under cyclic and random loading. *International Journal of Fatigue* 23(7). Elsevier: 643–652.

Łagoda T (2001) Energy models for fatigue life estimation under uniaxial random loading. Part I: The model elaboration. *International Journal of Fatigue* 23(6). Elsevier: 467–480.

Li DM, Nam WJ and Lee CS (1998) A strain energy-based approach to the low-cycle fatigue damage mechanism in a high-strength spring steel. *Metallurgical and Materials Transactions A 1998 29:5* 29(5). Springer: 1431–1439.

Li J, Wang X, Qi W, et al. (2019) Laser nanocomposites-reinforcing/manufacturing of SLM 18Ni300 alloy under aging treatment. *Materials Characterization* 153. Elsevier: 69–78.

Li JN, Gong SL, Liu KG, et al. (2019) Formation mechanism and mechanical properties of the selective laser melting Ni/Co base alloy. *Journal of Alloys and Compounds* 777. Elsevier: 963–967.

Liu D and Pons DJ (2017) Development of a stress-based creep-fatigue equation: Accommodating pure-fatigue to pure-creep for the high-cycle loading regime. *https://doi.org/10.1177/1056789517735678* 27(9). SAGE PublicationsSage UK: London, England: 1397–1415.

Macek W (2019) Fractal analysis of the bending-torsion fatigue fracture of aluminium alloy. *Engineering Failure Analysis* 99: 97–107.

For Peer Review

Macek W and Macha E (2015) The Control System Based on FPGA Technology For Fatigue Test Stand MZGS-100 PL. *Archive of Mechanical Engineering* 62(1).

Macek W and Mucha N (2017) Evaluation of Fatigue Life Calculation Algorithm of the Multiaxial Stress-Based Concept Applied to S355 Steel under Bending and Torsion. *Mechanics and Mechanical Engineering* 21(4): 935–951.

Macek W, Łagoda T and Mucha N (2017) Energy-based fatigue failure characteristics of materials under random bending loading in elastic-plastic range. *Fatigue and Fracture of Engineering Materials and Structures*. Epub ahead of print 2017. DOI: 10.1111/ffe.12677.

Macek W, Branco R, Costa JD, et al. (2021) Strain sequence effect on fatigue life and fracture surface topography of 7075-T651 aluminium alloy. *Mechanics of Materials* 160. Elsevier: 103972.

Macek W, Pejkowski Ł, Branco R, et al. (2022) Fatigue fracture surface metrology of thin-walled tubular austenitic steel specimens after asynchronous loadings. *Engineering Failure Analysis* 138. Pergamon: 106354.

Macek W, Robak G, Żak K, et al. (2022) Fracture surface topography investigation and fatigue life assessment of notched austenitic steel specimens. *Engineering Failure Analysis* 135. Pergamon: 106121.

Macek W, Tomczyk A, Branco R, et al. (2023) Fractographical quantitative analysis of EN-AW 2024 aluminum alloy after creep pre-strain and LCF loading. *Engineering Fracture Mechanics* 282. Pergamon: 109182.

Macoretta G, Bertini L, Monelli BD, et al. (2022) Productivity-oriented SLM process parameters effect on the fatigue strength of Inconel 718. *International Journal of Fatigue*. Elsevier: 107384.

Mandelbrot BB, Passoja DannE and Paullay AJ (1984) Fractal character of fracture surfaces of metals. *Nature* 308(5961): 721–722.

Milewski JO (2017) Additive Manufacturing of Metals. 258. Springer Series in Materials Science. Cham: Springer International Publishing.

Molski K and Glinka G (1981) A method of elastic-plastic stress and strain calculation at a notch root. *Materials Science and Engineering* 50(1). Elsevier: 93–100.

Mroziński S and Boroński D (2007) Metal tests in conditions of controlled strain energy density. *Journal of Theoretical and Applied Mechanics* 45.

Neuber H (1961) Theory of Stress Concentration for Shear-Strained Prismatical Bodies With Arbitrary Nonlinear Stress-Strain Law. *Journal of Applied Mechanics* 28(4). American Society of Mechanical Engineers Digital Collection: 544–550.

Newton L, Senin N, Gomez C, et al. (2019) Areal topography measurement of metal additive surfaces using focus variation microscopy. *Additive Manufacturing* 25. Elsevier: 365–389.

Podulka P (2021) The Effect of Surface Topography Feature Size Density and Distribution on the Results of a Data Processing and Parameters Calculation with a Comparison of Regular Methods. *Materials 2021, Vol. 14, Page 4077* 14(15). Multidisciplinary Digital Publishing Institute: 4077.

For Peer Review

Podulka P, Macek W, Branco R, et al. (2023) Reduction in Errors in Roughness Evaluation with an Accurate Definition of the S-L Surface. *Materials 2023, Vol. 16, Page 1865* 16(5). Multidisciplinary Digital Publishing Institute: 1865.

Ramberg W and Osgood WR (1943) Description of stress-strain curves by three parameters.

Romano S, Patriarca L, Foletti S, et al. (2018) LCF behaviour and a comprehensive life prediction model for AlSi10Mg obtained by SLM. *International Journal of Fatigue* 117. Elsevier: 47–62.

Santus C, Romanelli L, Grossi T, et al. (2022) Torsional-loaded notched specimen fatigue strength prediction based on mode I and mode III critical distances and fracture surface investigations with a 3D optical profilometer. *International Journal of Fatigue* 161. Elsevier: 106913.

Skibicki D and Pejkowski Ł (2017) Low-cycle multiaxial fatigue behaviour and fatigue life prediction for CuZn37 brass using the stress-strain models. *International Journal of Fatigue*. Epub ahead of print 2017. DOI: 10.1016/j.ijfatigue.2017.04.011.

Todhunter LD, Leach RK, Lawes SDA, et al. (2017) Industrial survey of ISO surface texture parameters. *CIRP Journal of Manufacturing Science and Technology* 19. Elsevier: 84–92.

Ye D, Matsuoka S, Suzuki N, et al. (2004) Further investigation of Neuber's rule and the equivalent strain energy density (ESED) method. *International Journal of Fatigue* 26(5). Elsevier: 447–455.

Zhu SP, Huang HZ, Ontiveros V, et al. (2011) Probabilistic Low Cycle Fatigue Life Prediction Using an Energy-Based Damage Parameter and Accounting for Model Uncertainty. *https://doi.org/10.1177/1056789511429836* 21(8). SAGE PublicationsSage UK: London, England: 1128–1153.

Zhu SP, Huang HZ, Li Y, et al. (2012) A Novel Viscosity-Based Model for Low Cycle Fatigue–Creep Life Prediction of High-Temperature Structures. *https://doi.org/10.1177/1056789511432789* 21(7). SAGE PublicationsSage UK: London, England: 1076–1099.

For Peer Review